UNDERSTANDING THE PERFORMANCE OF PROFILED COMPOSITE WALLS IN FIRE

Quang X. Le[1,2,*], Vinh T.N. Dao[2], Jose L. Torero[3]

[1] Faculty of Civil Engineering, The University of Danang – University of Science and Technology, Danang, Vietnam

[2] School of Civil Engineering, The University of Queensland, Brisbane, QLD, Australia

[3] Department of Civil, Environmental and Geomatic Engineering, University College London, UK

** Corresponding author.*

Email address: lxquang@dut.udn.vn

Abstract

To understand the performance of structural elements subject to one-side heating, the combined effects of temperature and temperature gradient (or the non-uniform temperature increase) must be accurately considered in developing structural performance models. However, due to insufficient consideration of such effects, the direct application of current understanding of general structural performance at high temperature on structural elements like profiled composite walls (PCWs) seems insufficient because of the complex role that the different materials can have in the presence of significant temperature gradients. Therefore, more research is needed to understand the performance of these structural elements when subjected to temperature increase and temperature gradients. Only then, the performance of PCWs at high temperature can be appropriately addressed. This paper presents and verifies a structural performance model that can be used to analyse the performance of PCWs subjected to combined thermal and mechanical loadings. First, details of an analytical study are presented, including thermal stress calculation within inhomogeneous and composite cross-section by fully considering the effects of non-uniform stiffness, non-linear temperature gradient, shifting of the neutral axis, and the coupling effects between stress and thermal expansion. Second, previously published experimental results into the performance of PCWs subjected to combined mechanical loading and one-side heating are then used to verify the newly-developed analytical model. It is also argued that the methodology for stress and curvature calculation developed in this study can be used to assess the performance of any structural elements (PCWs included) subjected to one-side heating. (244 words)

Keywords: thermal expansion; thermal bowing; thermal deflection; thermal reaction forces; thermal compressive stress; thermal shear stress.

NOMENCLATURE

V_A, V_B, H_A: reaction forces at supports A and B;

$\dot{q}''_{inc}$: incident heat flux on sample's surface;

x: distance from the reference axis to the fibre after deformation;

ε_0: normal strain at the reference axis;

$1/\rho$: curvature after deformation;

dA: small area of the cross-section at a distance of x from the reference axis;

h_{av}: position of the effective centroid;

PCWs: profiled composite walls;

N_u^{amb}: PCWs' axial load capacity at ambient temperature (kN);

$0.2N_u^{amb}$: an axial compressive load of $20\%N_u^{amb}$;

$0.4N_u^{amb}$: an axial compressive load of $40\%N_u^{amb}$;

HF42: an incident heat flux of 42 kW/m^2;

HF60: an incident heat flux of 60 kW/m^2;

TC(s): thermocouple(s).

1. Introduction

When structural elements like profiled composite walls (PCWs) are subjected to one-side heating, the transient heating results in a non-uniform increase of temperature as a function of time [1]. The non-linear evolution of temperature has a steep temperature gradient close to the heated surface and a much smaller temperature gradient close to the unheated region [2, 3]. Meanwhile, the temperature increase in structural elements generally leads to the reduction of material properties (i.e., Young's modulus and compressive strength) and induces restrained thermal deformation [4-6]. The results of this non-uniform temperature increase are the non-uniform distribution of the mechanical properties, thermal bowing, coupled effects of stress and thermal expansion, and the shift of the effective centroid away from the plane of symmetry [7-9]. Such effects of the temperature and temperature gradient on structural elements must be taken into account when developing structural performance models.

When addressing the fundamental principles of structural behaviour under thermal effects, Usmani *et al.* [7] used the effective strain, which is the linear combination of thermal expansion strain and thermal bowing strain. This approach highlighted the response of structural elements subjected to temperature increases and temperature gradients and the effects of thermal expansion and thermal gradients. However, a major limitation of this work is the assumption of a uniform Young's modulus distribution (i.e. no consideration of the non-uniform distribution of the Young's modulus due to the temperature gradient.) Thus, the shift of the centre of stiffness (or the effective centroid) was not fully considered. Garlock *et al.* [8], on the other hand, did not separate the effects of non-uniform temperature increase (i.e., temperature and temperature gradient) but divided the cross-section into fibres linked by strain compatibility conditions and considered the non-uniform distribution of stiffness. The total strain caused by stress and temperature was then calculated for every single fibre. This work, therefore, described the mechanics of the performance of structural elements subjected to axial load and thermal gradients by considering the shift of the section’s effective centroid toward the colder region. One of the limitations of this work is that it did not discriminate the transient thermal strain of solid materials (i.e., steel, concrete) when subjected to thermal and mechanical loads simultaneously. It is notable that none of the discussed works considers the coupled effects between thermal expansion and stress on the whole cross-section as the thermal stresses developed due to the combined effects of temperature increases and temperature gradients [7, 8, 10, 11]. Further information of the effects of temperature, temperature gradient on structural elements can be found in the following references[3, 7, 12].

Meanwhile, the coupled effects between stress and thermal expansion have long been incorporated into the total strain models of concrete when subjected to thermal and structural loading by introducing the load-induced thermal strain (LITS) [6, 10, 13-16]. This aspect of strain was incorporated in the analysis of concrete walls subjected to one-sided thermal loading by Pham *et al.* [9]. However, this work failed to define the shift of the centre of stiffness (or effective centroid), thus did not properly consider the moment equilibrium conditions. Consequently, the stress profile calculated by this approach delivered tensile stress in the middle area of the cross-section, although the structural element was subjected to one-side heating.

When analysing the performance of such structural elements as profiled composite walls (PCWs) at high temperatures, it is important to understand performance at such high temperatures of its components (i.e., concrete core, profiled steel sheeting), the interaction between the concrete core and the steel sheets, and the potential effects of any studs or reinforcement [17-20]. Although many studies have been done to understand the performance of PCWs at ambient temperature, research on understanding their behaviour at high temperatures is still limited.

Furthermore, the direct application of current understanding of general structural performance at elevated temperatures on PCWs seems insufficient because of the composite nature of these systems and the complex role that the different materials can have in the presence of significant temperature gradients [1, 2, 21].

Thus, more research is needed to understand the performance of these structural elements when subjected to temperature increases and temperature gradients. Only then, the performance of PCWs at high temperature can be appropriately addressed. The following influencing factors should therefore be taken into account, including (i) mechanical properties evolutions at high temperature, (ii) the shift of the effective centroid, (iii) the coupled effect between stress and thermal expansion into the thermal expansion strain (ε_0), and (iv) the curvature of a structural element ($1/\rho$). The stress distribution within the cross-section can then be calculated for different structural boundary conditions.

This paper presents and verifies an analytical model for the performance of PCWs in fire. In the analytical model, the coupled effects of stress and thermal expansion and the effects of temperature and temperature gradient on materials and structures can be effectively considered. First, the analytical study includes details of thermal stress calculation within inhomogeneous and composite cross-section by fully considering the effects of uneven stiffness, non-linear temperature gradient, shifting of the neutral axis, and the coupled effects between stress and thermal expansion. The subsequent section describes an experimental program into the performance of PCWs subjected to combined mechanical loading and one-side heating, providing quantitative data of thermal and mechanical behaviour of PCWs under different thermal-structural boundary conditions at high temperatures. Finally, the experimental results are used to verify the analytical model. While this study focuses on PCWs, the methodology for stress and curvature calculation developed therein can be used to understand the performance of any structural elements subjected to one-side heating.

2. Response of structural element subjected to one-side heating condition

In this section, the analytical model used to analyse the response of structural elements subjected to one-sided heating is explained in detail. The structural element is assumed to comply with the Bernoulli-Euler beam theory that means a plane cross-section perpendicular to the longitudinal axis before subjected to thermal loading remains a plane cross-section perpendicular to the deformed longitudinal axis after thermal loading [22].

As the temperature increases non-uniformly within the cross-section, the Young's modulus is no longer uniform over the cross-section. The cross-section of the structural element could then be considered as a heterogeneous material or a composite of different layers. Two analytical models are developed for the heterogeneous material and composite cross-section. The model of the composite cross-section is then chosen to calculate the thermal expansion strain (ε_0) and the curvature ($1/\rho$) in the case of the experimental study. The thermal stress profile and subsequent thermal expansion force are then calculated. It should be noted that the effects of temperature and temperature gradient, thermal expansion, thermal bowing, and the coupled effects between stress and thermal expansion are fully considered in both analytical models.

2.1. Thermal stress in unconstrained conditions

a. Thermal stresses in heterogeneous structural elements

When subjected to non-uniform temperature distributions, the Young's modulus distribution within a structural elements cross-section is no longer uniform [6]. Let us consider a structural element, simply-supported as shown in Figure 1, subjected to one-sided thermal loading ($\dot{q}''_{inc}$).

Thus, the structural element will be deformed and bow toward the heating source in the absence of reaction forces at the supports (refer to Figure 1). The behaviour of the structural element in this case contains two aspects, (i) axial elongation and (ii) bending due to the temperature difference in the x-direction. Also, the effective centroid of the cross-section moves toward the colder region due to the non-uniform Young's modulus distribution within the cross-section. The longitudinal axis passing through the new effective centroid position elongates to *e'f'* > *ef* because of the combined effects of axial elongation and non-uniform Young's modulus distribution within the cross-section.

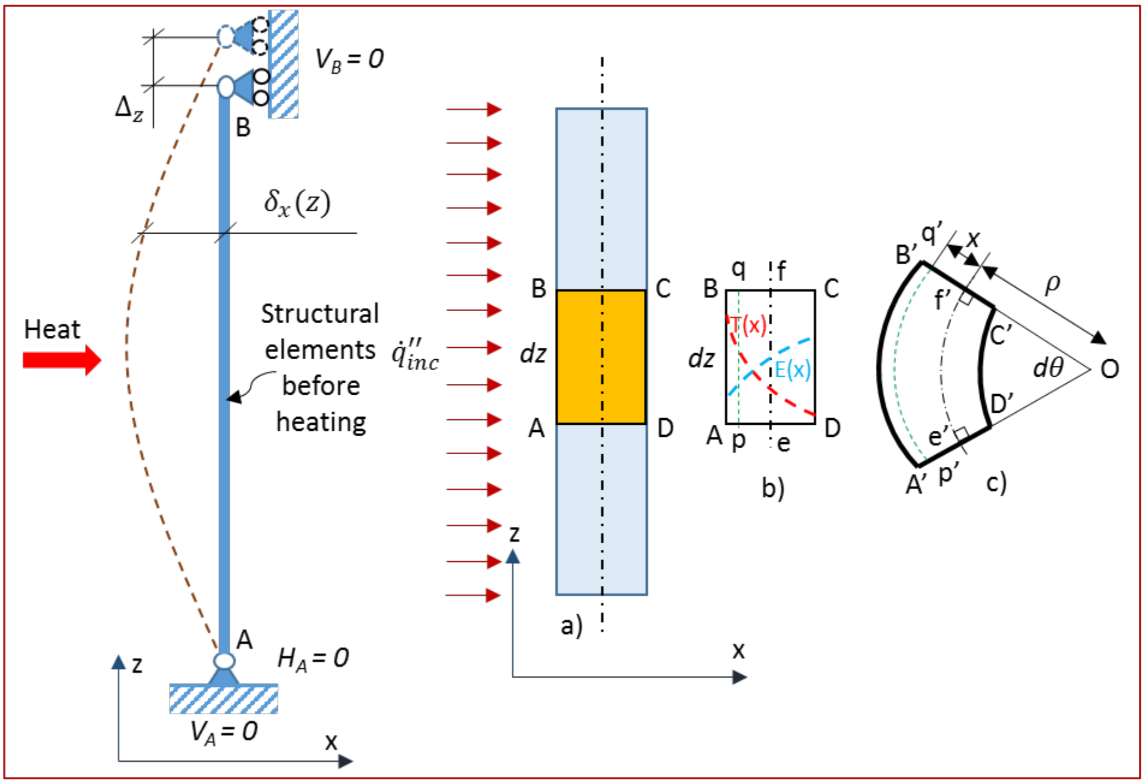

Figure 1. One-side heated structural element: a) Thermal boundary condition; b) Temperature distribution and Young's modulus distribution in the infinitesimally small width dz; and c) Thermal deformation with the infinitesimally small dz.

The longitudinal axis passing through the new effective centroid position of the cross-section is now chosen as the reference axis for subsequent calculations because the applied axial load on the effective centroid produces only pure axial stress with no bending [8]. The strain $\varepsilon_z(x)$ at a distance of *x* from the *reference* axis after deformation can be calculated as:

Equation 1

$$\begin{aligned}\varepsilon_z(x) = \frac{p'q'-pq}{pq} = \frac{p'q'-ef}{ef} &= \frac{(p'q'-e'f')+(e'f'-ef)}{ef} \\ &= \frac{e'f'-ef}{ef} + \frac{p'q'-e'f'}{ef} = \varepsilon_0 + \frac{p'q'-e'f'}{ef} \\ &= \varepsilon_0 + \frac{(x+\rho)d\theta - \rho d\theta}{ef} \\ &= \varepsilon_0 + \frac{(x+\rho)d\theta - \rho d\theta}{\rho d\theta}.\frac{\rho d\theta}{ef} = \varepsilon_0 + \frac{x}{\rho}.\frac{\rho d\theta}{ef} \\ &= \varepsilon_0 + \frac{x}{\rho}.\left(\frac{ef + \rho d\theta - ef}{ef}\right) = \varepsilon_0 + \frac{x}{\rho}.(1+\varepsilon_0) \\ &= \varepsilon_0 + \frac{x}{\rho} + \varepsilon_0\frac{x}{\rho} \cong \varepsilon_0 + \frac{x}{\rho}\end{aligned}$$

The $\varepsilon_z(x)$ can thus be simplified by the following equation:

Equation 2

$$\varepsilon_z(x) = \varepsilon_0 + \frac{x}{\rho}$$

where *x* is the distance from the *reference* axis to the fibre after deformation, ε_0 is the normal strain at the *reference* axis (*x* = 0), and $1/\rho$ is the curvature (*x* = 0) after deformation. The deformation and movement of the *reference* axis can be seen in Figure 1.

The total strain at a distance *x* from the reference axis must consider the coupled effect between stress and expansion; thus, the strain at a distance from the *reference* axis should be [11]:

$$\varepsilon_z(x) = \frac{\sigma_z(x)}{E(T)} + \alpha_0.\Delta T(x) - \frac{\sigma_z(x)}{E^2(T)}.\frac{\partial E}{\partial T}.\Delta T(x)$$

Equation 3

$$= \frac{\sigma_z(x)}{E(x)} + \alpha_0.\Delta T(x) - \frac{\sigma_z(x)}{E^2(x)}.\frac{\partial E}{\partial T}.\Delta T(x)$$

By directly comparing Equations 2 and 3 , we obtain:

Equation 4 $$\varepsilon_0 + \frac{x}{\rho} = \frac{\sigma_z(x)}{E(x)} + \alpha_0.\Delta T(x) - \frac{\sigma_z(x)}{E^2(x)}.\frac{\partial E}{\partial T}.\Delta T(x)$$

By re-arranging the stress and defining effective Young's modulus, we obtain:

Equation 5 $$\varepsilon_0 + \frac{x}{\rho} = \sigma_z(x)\left(\frac{1}{E(x)} - \frac{1}{E^2(x)}.\frac{\partial E}{\partial T}.\Delta T(x)\right) + \alpha_0.\Delta T(x)$$

and

Equation 6 $$\varepsilon_0 + \frac{x}{\rho} = \frac{\sigma_z(x)}{E_{eff}(T)} + \alpha_0.\Delta T(x)$$

where $E_{eff}(x)$ is the effective Young's modulus, which can be calculated as follows:

Equation 7 $$\frac{1}{E_{eff}(x)} = \frac{1}{E(x)} - \frac{1}{E^2(x)}\frac{\partial E}{\partial T}\Delta T(x)$$

The stress at a distance *x* from the reference axis can be then calculated by solving Equation 8:

Equation 8 $$\sigma_z(x) = E_{eff}(x)\left(\varepsilon_0 + \frac{x}{\rho} - \alpha_0.\Delta T(x)\right)$$

The unknown parameters in Equation 8 are ε_0 and $1/\rho$. Since the structural element is in simply-supported restraint condition and free from external forces, the equilibrium of force (refer to Equation 9 and that of moment (Equation 10) give the following relations:

Equation 9 $$\int_A \sigma_z(x)dA = 0$$

and

Equation 10 $$\int_A \sigma_z(x)x dA = 0$$

where dA is a small element area of the cross-section at a distance of *x* from the *reference* axis. By substituting Equation 8 into Equations 9 and 10, we obtain the axial strain ε_0 and the curvature $1/\rho$ at the *reference* axis ($x = 0$), as follows:

Equation 11 $$\varepsilon_0 = \frac{P_T I_{E2} - M_T I_{E1}}{I_{E0} I_{E2} - I_{E1}^2}$$

and

Equation 12 $$\frac{1}{\rho} = \frac{M_T I_{E0} - P_T I_{E1}}{I_{E0} I_{E2} - I_{E2}^2}$$

where,

Equation 13 $$I_{E0} = \int_A E_{eff}(x)dA$$

Equation 14 $$I_{E1} = \int_A E_{eff}(x)xdA$$

Equation 15 $$P_T = \int_A \alpha_0 \Delta T(x) E_{eff}(x)dA$$

Equation 16 $$I_{E2} = \int_A E_{eff}(x).x^2 dA$$

Equation 17 $$M_T = \int_A \alpha_0 \Delta T(x) E_{eff}(x).xdA$$

It should be noted that a similar derivation for Equations 9 to 17 can be found in Hetnarski *et al.* [23], Obata [24] and Malzbender [25]. In these studies, they investigated the thermal stresses in heterogeneous or multilayer beams. However, these studies did not take into account effects of the shift of the effective centroid towards the colder region due to the non-uniform distribution of Young's modulus within the cross-section.

By substituting Equations 11 and 12 into Equation 8, the thermal stress distribution in the cross-section can be then calculated as:

Equation 18
$$\sigma_z(x) = E_{eff}(x)\left(\frac{P_T I_{E2} - M_T I_{E1}}{I_{E0} I_{E2} - I_{E1}^2} + x.\frac{M_T I_{E0} - P_T I_{E1}}{I_{E0} I_{E2} - I_{E2}^2} - \alpha_0.\varDelta T(x)\right)$$

b. Thermal stresses in composite structural element

Now considering the structural element contains three homogeneous layers in which $E_1 < E_2 < E_3$. A parametric study was conducted looking at the least number of layers required. It was observed that a three-layer composite structural element was capable of reproducing the test data. This will be explained in more detail in subsequent sections. While multiple layers could potentially increase accuracy, for this study only three layers will be utilised. This will also avoid having layers smaller than the maximum size of the aggregate. This calculation can be generalised for other composite structural elements that contain two layers or more than three layers.

Figure 2 shows the mechanism of the composite cross-section with the thicknesses of each layer, being h_1, (h_2-h_1), and (h-h_2). The reference axis used for subsequent calculation is the longitudinal axis that passes through the new effective centroid which is shifted toward the colder region due to the non-uniform distribution of Young's modulus as shown in Figure 3.

The solid is divided into layers that can be assigned a mean temperature. The mean value of the temperature of a layer is taken to calculate Young's modulus. As the coupled effect between stress and expansion must be taken into account, the effective Young's modulus for each layer is calculated as follows:

Equation 19
$$E_{eff}^i = \frac{1}{\frac{1}{E^i} - \frac{1}{{E^i}^2}\frac{\partial E^i}{\partial T}\Delta T_{av}^i}$$

where E^i is the average Young's modulus at each layer (*i = 1, 2, 3*).

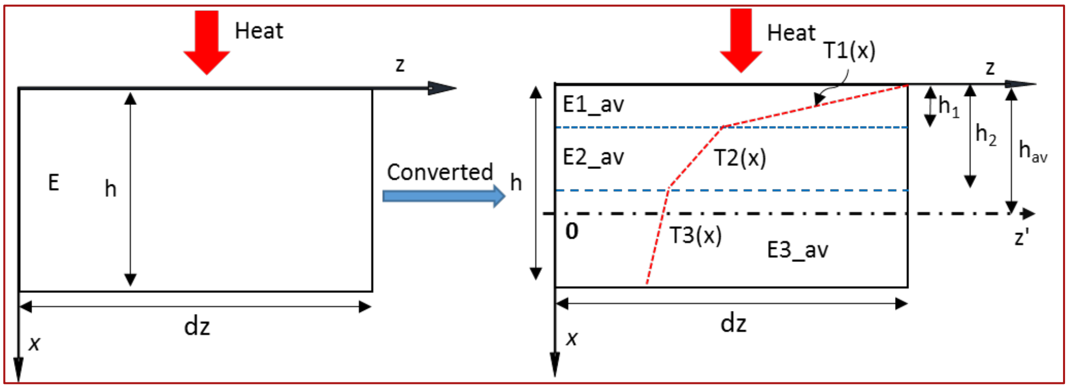

Figure 2. Original and converted cross-section with the assumption for the following calculation that $h_{av} > h_2$.

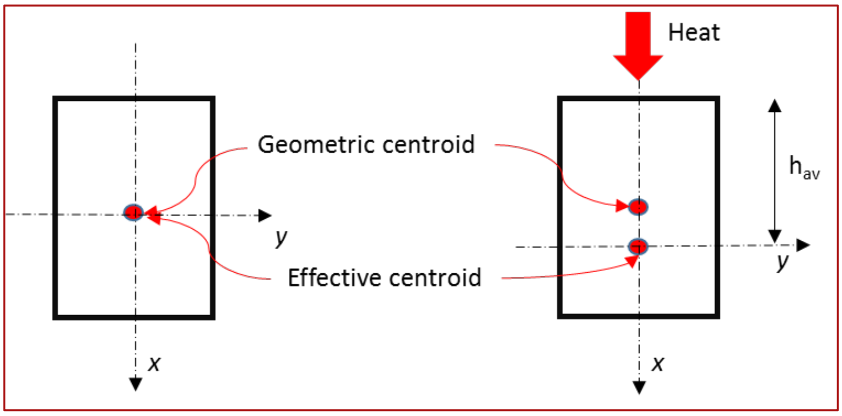

Figure 3. The shift of the effective centroid due to the non-uniform distribution of Young's modulus in samples' cross-section.

To simplify the calculation while complying with the strain compatibility of Bernoulli-Euler theory, the equivalent area method is employed to calculate the thermal stress within the cross-section. In the following calculation, the cross-sections of Layers 1 and 2 are converted into the cross-section of Layer 3 by using modular ratios to create a homogeneous material within the cross-section. The modular ratios for each layer are as follows:

Equation 20 $$n_1 = \frac{E_{eff}^1}{E_{eff}^3}; n_2 = \frac{E_{eff}^2}{E_{eff}^3}$$

The whole cross-section is now considered having a single material of Layer 3. Assuming the thickness of each layer is unchanged, the width of Layers 1 and 2 with Young's modulus of E_3 are $n_1 . b$ and $n_2 . b$, respectively. Thus, $A_1 = n_1 b . h_1$; $A_2 = n_2 b . h_2$

The position of the effective centroid and thus the *reference* axis from the *z*-axis can be calculated as:

Equation 21 $$h_{av} = \frac{h_1 . n_1 A_1 + h_2 . n_2 A_2 + h_3 A_3}{A_1 + A_2 + A_3}$$

where, h_1, h_2, and h_3 are the distances from the centroid of A_1, A_2, and A_3 to the z-axis as shown in Figure 2. The reference axis is now assumed at *z'* as shown in Figure 3.

The axial strain ε_0 and the curvature $1/\rho$ at the reference axis ($x = 0$) can be then calculated:

Equation 22 $$\varepsilon_0 = \frac{P_T I_{E2} - M_T I_{E1}}{I_{E0} I_{E2} - I_{E1}^2}$$

and

Equation 23 $$\frac{1}{\rho} = \frac{M_T I_{E0} - P_T I_{E1}}{I_{E0} I_{E2} - I_{E2}^2}$$

in which,

Equation 24
$$I_{E0} = E_{eff}^{3}(n_1 b h_1 + n_2 b(h_2 - h_1) + b(h_3 - h_2)$$

Equation 25
$$I_{E1} = E_{eff}^{3}\left(\int_{-h_{av}}^{-(h_{av}-h_1)} n_1 b\, dx + \int_{-(h_{av}-h_1)}^{-(h_{av}-h_2)} n_2 b\, dx + \int_{-(h_{av}-h_2)}^{h_3-h_{av}} b\, dx\right)$$

Equation 26
$$P_T = E_{eff}^{3}\left(\int_{-h_{av}}^{-(h_{av}-h_1)} n_1 b\, \alpha_0 \varDelta T(x) dx + \int_{-(h_{av}-h_1)}^{-(h_{av}-h_2)} n_2 b\, \alpha_0 \varDelta T(x) dx + \int_{-(h_{av}-h_2)}^{h_3-h_{av}} b \alpha_0 \varDelta T(x)\, dx\right)$$

Equation 27
$$I_{E2} = E_{eff}^{3}\left(\int_{-h_{av}}^{-(h_{av}-h_1)} n_1 b\, x^2 dx + \int_{-(h_{av}-h_1)}^{-(h_{av}-h_2)} n_2 b\, x^2 dx + \int_{-(h_{av}-h_2)}^{h_3-h_{av}} b x^2\, dx\right)$$

Equation 28
$$M_T = \int_A \alpha_0 \varDelta T(x) E_{eff}(x).x dA = E_{eff}^{3}\left(\int_{-h_{av}}^{-(h_{av}-h_1)} n_1 b\, \alpha_0 \varDelta T(x).x dx + \int_{-(h_{av}-h_1)}^{-(h_{av}-h_2)} n_2 b\, \alpha_0 \varDelta T(x).x dx + \int_{-(h_{av}-h_2)}^{h_3-h_{av}} b \alpha_0 \varDelta T(x).x\, dx\right)$$

231 The stress distribution within the cross-section is as follows:

Equation 29 $$\sigma_z(x) = E_{eff}^3\left(\frac{P_T I_{E2} - M_T I_{E1}}{I_{E0} I_{E2} - I_{E1}^2} + x.\frac{M_T I_{E0} - P_T I_{E1}}{I_{E0} I_{E2} - I_{E2}^2} - \alpha_0.\Delta T(x)\right)$$

When the axial force, P_M, and the mechanical bending, M_M, act on the column/wall, the axial strain and the curvature can be calculated as:

Equation 30 $$\varepsilon_0 = \frac{P I_{E2} - M I_{E1}}{I_{E0} I_{E2} - I_{E1}^2}$$

and

Equation 31 $$\frac{1}{\rho} = \frac{M I_{E0} - P I_{E1}}{I_{E0} I_{E2} - I_{E2}^2}$$

where,

Equation 32 $$P = P_M + P_T$$

Equation 33 $$M = M_M + M_T$$

After calculating the stress profile on the converted cross-section by Equation 29, the thermal stress needs to be converted into the original cross-section, which has three layers with different Young's modulus values. Thus, the calculated thermal stresses on Layers 1 and 2 must be multiplied by the modular ratios, n_1 and n_2, respectively.

2.2. Thermal behaviour of structural elements with various structural boundary conditions

Common structural boundary conditions for vertical structural elements can be easily taken into account, including (a) Pinned-pinned ends; (b) Fixed-simply pinned ends; (c) Fixed-pinned ends; (d) Fixed-slide ends; and (e) Fixed-fixed ends. Figure 4 shows the reaction forces and deflection of vertical elements subjected to one-side heating and mentioned structural boundary conditions from (a) to (e). The reaction forces can be calculated by using the method of superposition. The structural element is under statically indeterminate to the first degree. If the unknown forces are removed, the statically determinate system is obtained. This system subjected to heat only is called primary system or “0”-system as shown in Figure 4. The statically determinate system subjected to unknown forces (X_1, X_2, X_3) is considered as “1”-system with the removed support B. These forces correspond to the unknown support reaction at B in the original system. The original system can be then calculated as a superposition of the systems “0” and “1” as illustrated in Figure 4 and Table 1.

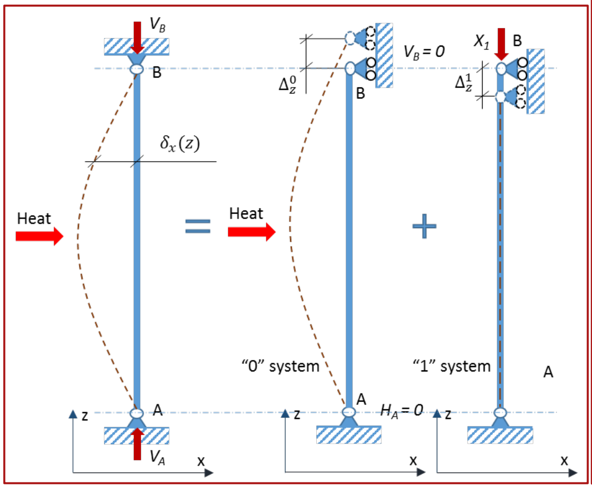

a) Pinned-pinned ends;

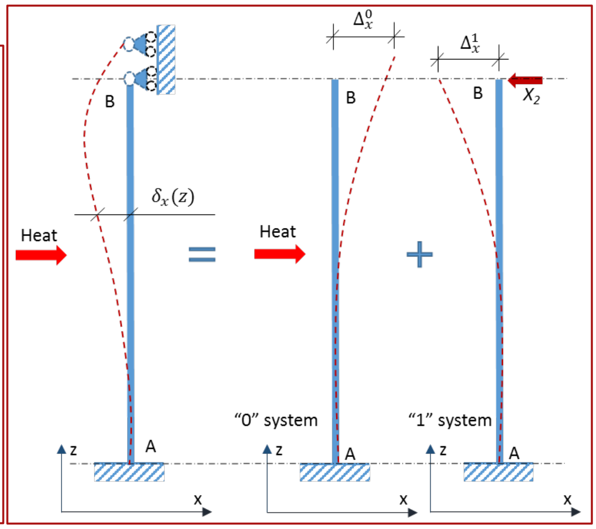

b) Fixed-simply pinned ends;

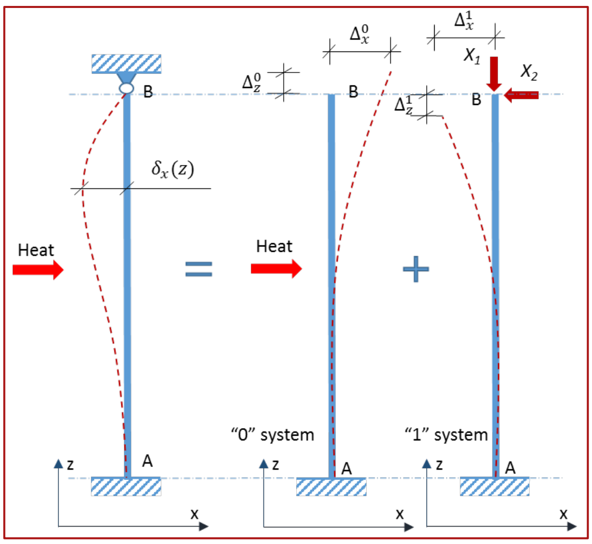

c) Fixed-pinned ends;

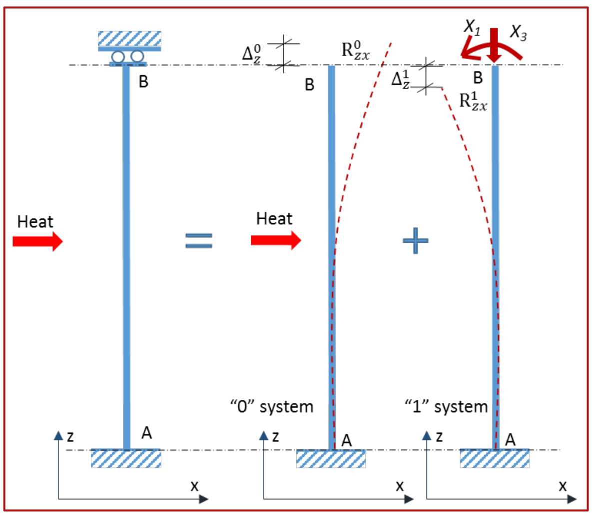

d) Fixed–slide ends;

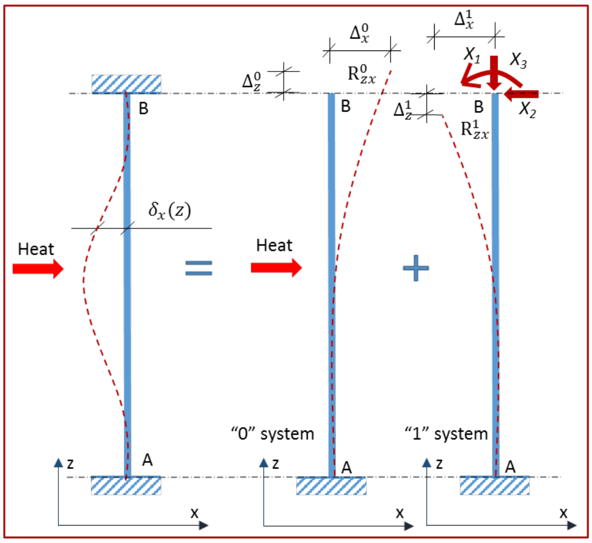

e) Fixed-fixed ends.

Figure 4. Combined thermal and structural boundary conditions.

The curvature of the structural elements ($1/\rho$) with structural boundary conditions and one-side heating will be:

Equation 34
$$\frac{1}{\rho} = \frac{M_T I_{E0} - P_T I_{E1}}{I_{E0} I_{E2} - I_{E2}^2}$$

The following calculation does not consider the effects of the axial force, P_M, and the moment, M_M, acting on column/wall when subjecting to thermal loading. The reaction forces at the supports and deflection profile for each case are summarised in Table 1.

Table 1. Solution for the reaction forces at supports.

Type of supports	*X_1*	*X_2*	*X_3*
Pinned-pinned	$\int_A E_{eff}^3(x)\left(x.\frac{M_T I_{E0} - P_T I_{E1}}{I_{E0} I_{E2} - I_{E2}^2} - \alpha_0.\Delta T(x)\right) dA$	*0*	*0*
Fixed-simply pinned	*0*	$\frac{3M_T}{2L}$	*0*

Type of supports	X_1	X_2	X_3
Fixed-pinned	$\int_A E^3_{eff}(x)\left(x.\frac{M_T I_{E0} - P_T I_{E1}}{I_{E0} I_{E2} - I^2_{E2}} - \alpha_0.\Delta T(x)\right) dA$	$\frac{3M_T}{2L}$	*0*
Fixed-slide	$\int_A -\alpha_0.\Delta T(x) E_{eff}(x) dA$	*0*	$-M_T$
Fixed-fixed	$\int_A -\alpha_0.\Delta T(x) E_{eff}(x) dA$	0	$-M_T$

3. Experimental study into performance of PCWs subject to mechanical and thermal loadings

This section briefly summarizes the relevant information of a previously published experimental study into performance of PCWs subjected to mechanical and one-side heating. Details of the experimental setup can be found at Le *et al.* [26]. The results of this experimental study are used to verify the analytical study developed in this study.

3.1. Experimental details

The tested sample size was 290 mm (width) x 400 mm (height) x 80 mm (thickness) and was designed as a short wall with an average compressive load capacity of the PCWs of 526 kN at ambient temperature. Samples were heated using two incident heat flux levels of magnitude consistent within residential fires (42 kW/m^2 and 60 kW/m^2) [27]. To measure the temperature distribution, thermocouples were embedded within the sample's cross-section before casting, as shown in *Figure* 5.

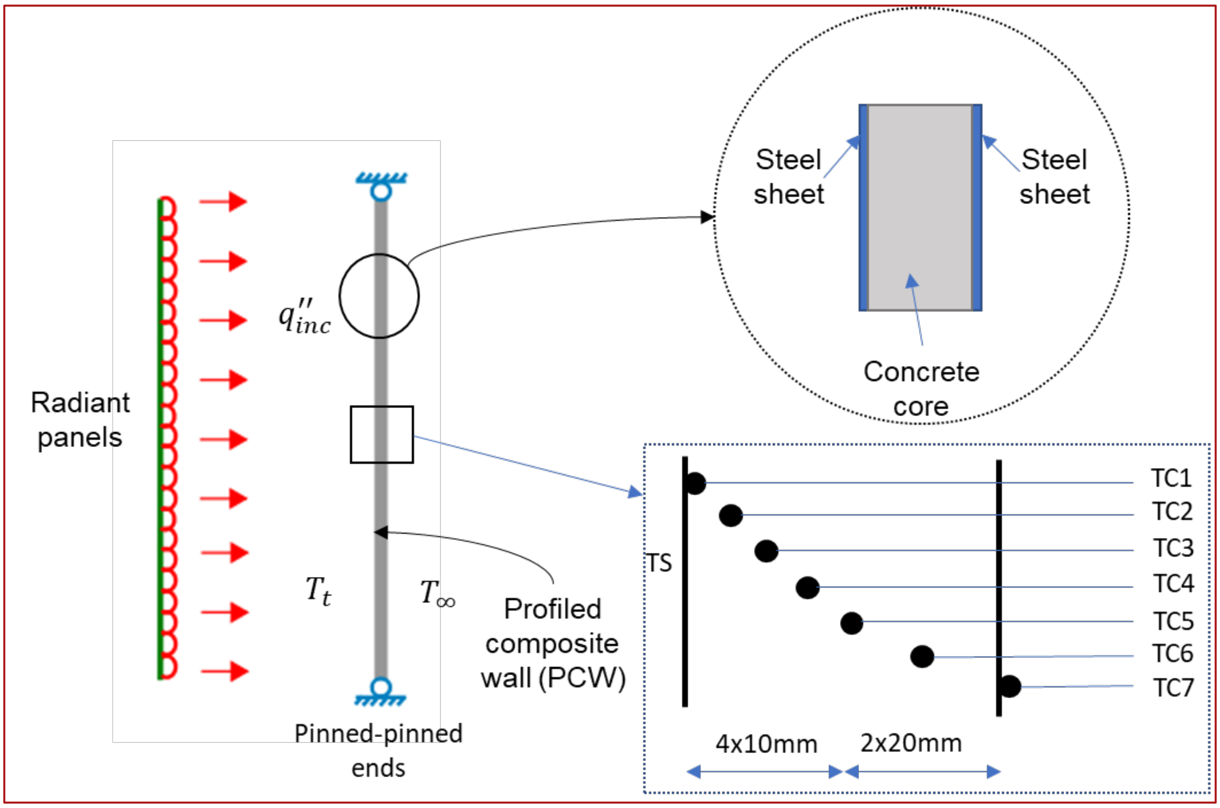

Figure 5. Experimental schematic with thermal-structural boundary condition, PCWs' cross-section, and thermocouples' positions.

Figure 5 also shows the heating-loading test setup for PCWs. Samples were subjected to different concentric and eccentric loads before heating. The structural boundary condition was maintained by using 1MN MTS machine to create pinned-pinned ends on all tested samples' heads. This structural boundary condition was maintained unchanged to record the thermal expansion force during the heating period. The target heating time was 90 min for both incident heat flux levels. After the 90-min heating period, samples were loaded until failure. In cases where severe spalling occurred, the heating was stopped, and samples were immediately subjected to loading (Tests 2-7, 2-8, 2-11, and 2-12). Details of the different testing conditions have been summarized in Table 2.

Table 2. Summary of test conditions.

Test name	Initial compressive load (kN)	Incident heat flux (kW/m^2)	Eccentricity (mm)	Heating time (min)
2-5	0	42	0	90
2-6	0	42	0	90
2-7	$0.4N_u^{amb}$	42	0	90 min or after spalling
2-8	$0.4N_u^{amb}$	42	0	90 min or after spalling
2-9	$0.2N_u^{amb}$	42	10	90
2-10	$0.2N_u^{amb}$	42	10	90
2-11	0	60	0	90 or after spalling
2-12	0	60	0	90 or after spalling
2-13	$0.2N_u^{amb}$	60	0	90
2-14	$0.2N_u^{amb}$	60	0	90
2-15	$0.2N_u^{amb}$	60	0	90

3.2. Thermal characterisation of the specimens

Given the importance of the temperature gradients on the behaviour of the PCW's, it is essential to provide here a brief summary of the temperature measurements presented by Le et al. [26]. Figures 6 and 7 show the spatially averaged temperature history of the three layers. The data shows that the temperature gradient between the depth of 10 mm and 20 mm (from the heated surface) gradually increased when heating started and then stabilised after 20 min of heating. In contrast, the temperature gradient between the depth of 20 mm and 30 mm remained constant at around 5 °C/mm for the first 30 min after heating started. After 30 min, the gradient significantly increased up to 10 °C/mm in the sample heated by HF42 and 15°C/mm in the sample heated by HF60. However, for both heat-fluxes, the temperature gradient within Layer 1 and Layer 2 remained unchanged after 30 min of heating (Figure 8). The temperature and temperature gradient in Layer 3 increased slowly during most of the heating duration (Figures 6 and 7).

For the samples subjected to HF42, explosive spalling occurred at around 60 min from the onset of heating. As soon as the spalling occurred, a significant difference occurred between the temperature gradient on Layer 1, Layer 2, and Layer 3, and the average temperature on Layer 1 (~450 °C) was triple the average temperature of Layer 3 (~150 °C) (refer to Figures 6 and 7). In the rest of the spalled samples, the temperature gradient in the first layer was significantly high, while the temperature of the other regions remained cold (Figure 8).

These observations on the temperature gradients serve to verify the separation of the analytical formulation into three distinct layers with different behaviour (Figure 2).

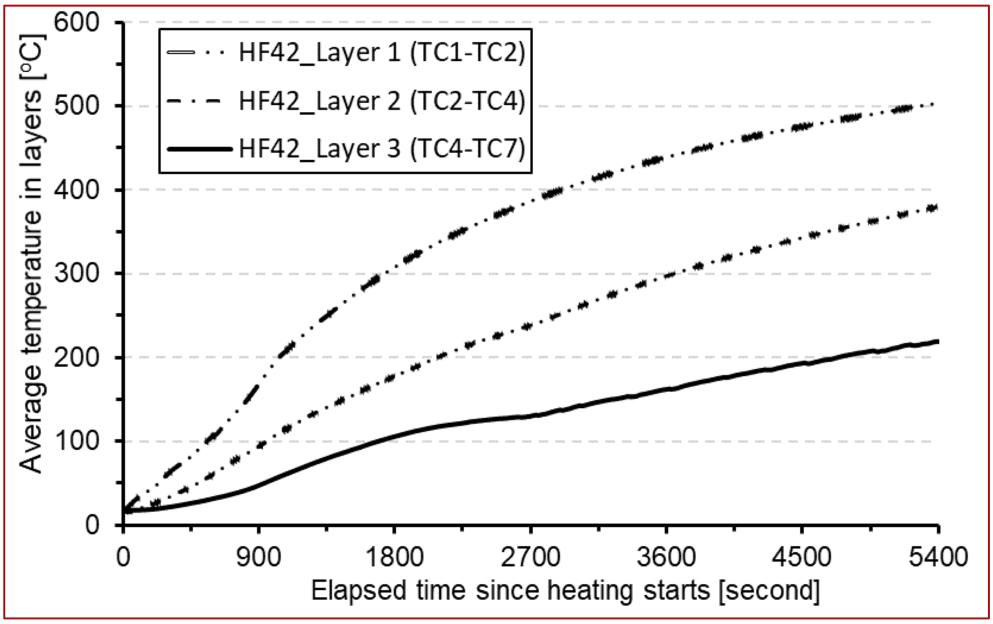

Figure 6. Average temperature increases in each layer of samples heated by HF42, calculated based on temperature recorded by TCs in Le et al. [26].

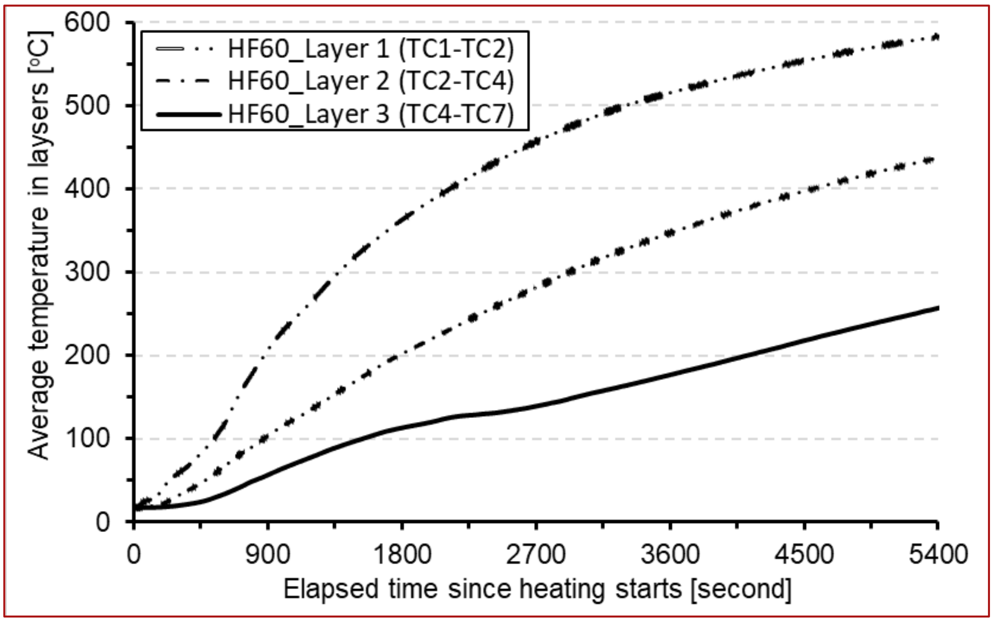

Figure 7. Average temperature increases in each layer of samples heated by HF60, calculated based on temperature recorded by TCs in Le et al. [26].

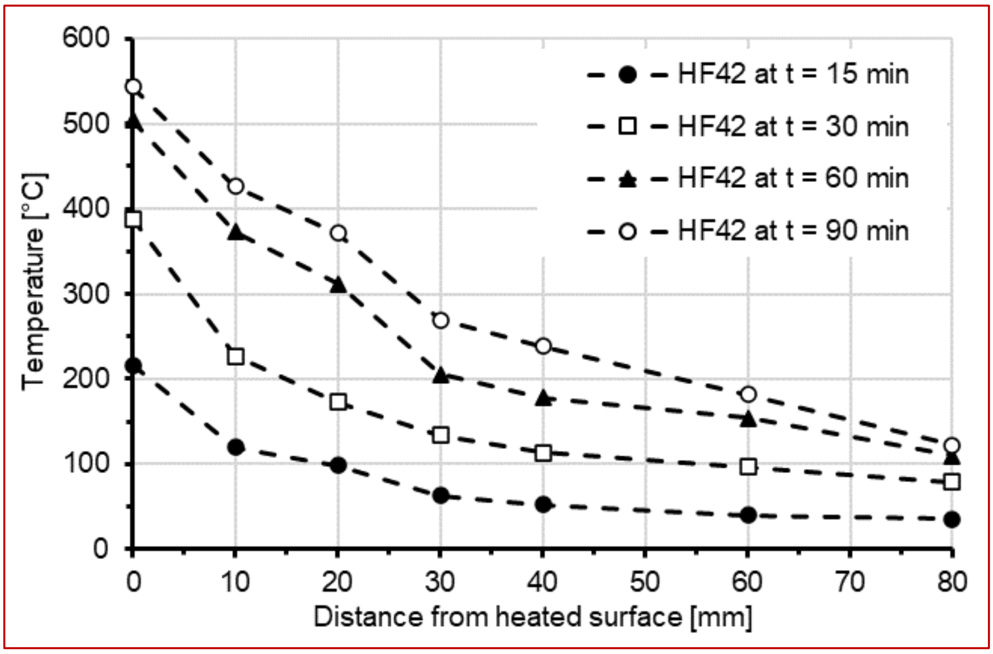

a) Incident heat flux of 42 kW/m^2.

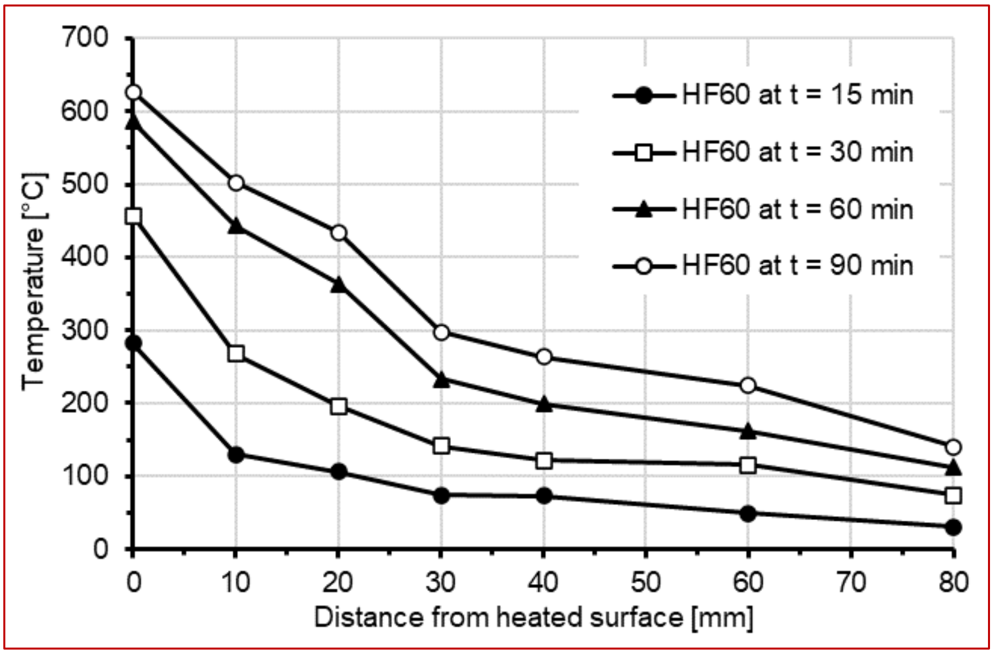

b) Incident heat flux of 60 kW/m^2.

Figure 8. Temperature profiles of the samples heated by incident heat fluxes of 42 and 60 kW/m^2 at 15, 30, 60 and 90 minutes [26].

3.3. Mechanical properties of concrete

As can be seen from Figure 8, the temperature of steel skin on the heated side rapidly increased since the radiant panel was turned on. Its temperature reached to 550 °C in the first 15 minutes when samples were heated by 60 kW/m^2, then reached to 700 °C after 1.5 hours heating. At this range of temperature, the Young's modulus of steel reduced by 60 to 90 % of its original Young's modulus at ambient temperature [6]. In addition, the cross-section area of the steel skins was much smaller than that of concrete area. Consequently, the thermal expansion force created by steel skin was significantly smaller relative to that by the concrete core, thus deemed negligible in the total thermal expansion forced recorded in the test. Therefore, the steel skin thermal expansion force was neglected during the calculation process.

Based on the experimental observation in Section 3.2, the cross-section of concrete is divided into three layers, including: Layer 1 (0 – 10 mm), Layer 2 (10 – 30 mm), and Layer 3 (30 – 80 mm). Also, the average temperature is considered as the representative temperature of the non-uniform temperature distribution within each layer. Basically, the sample's cross-section should be divided into as many layers as possible to increase the accuracy of calculation; however, each layer should not be smaller than the maximum aggregate size, which is 10 mm in this experimental study.

As the cross-section is divided into three layers, the mechanical properties are, therefore, assumed to be only homogeneous within each layer and represented by the mechanical properties at the average temperature of each layer. Consequently, the cross-section of the PCWs can be considered as a composite cross-section of three layers of concrete, which have different Young's modulus values. The Young's modulus of concrete for each layer is calculated based on its average temperature recorded from the experimental study. The correlations for mechanical properties of concrete at high temperature were selected based on the correlations available in the published literature:

- Two relationships of Young's modulus and temperature are used to calculate the thermal stress developed in this study: (i) The proposed model given in Aslani *et al.* [28]; (ii) the Young's modulus and temperature relationship developed by using regression analysis (*Equation 35*) from the tests conducted by Diederichs *et al.* [29]. The correlation developed from the test data conducted by Diederichs *et al.* [29] is considered as *the lower bound*, while the correlation developed by Aslani *et al.* [28] is considered as *the upper bound* values for the calculation purposes as shown in Figures 10 to 14. Figure 9 shows the reduction of Young's modulus in each concrete layer of samples heated by HF42 and HF60 using *Equation 35*.

Equation 35 $$E(T) = E_0(1.656 \times 10^{-6}T^2 - 2.554 \times 10^{-3}T + 1.002)$$

- The compressive strength and temperature relationship are chosen from European Standard [6];
- Figure 9 shows the calculated ratio of the Young's modulus at elevated temperatures to ambient temperature of each layer (1, 2, 3) in two heating scenarios of HF42 and HF60;

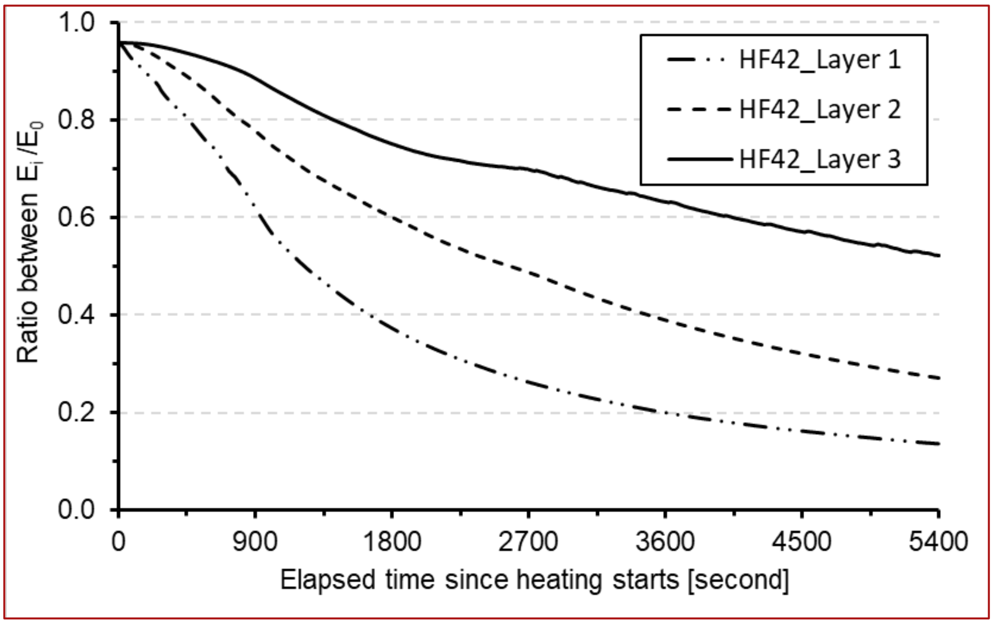

a) HF42.

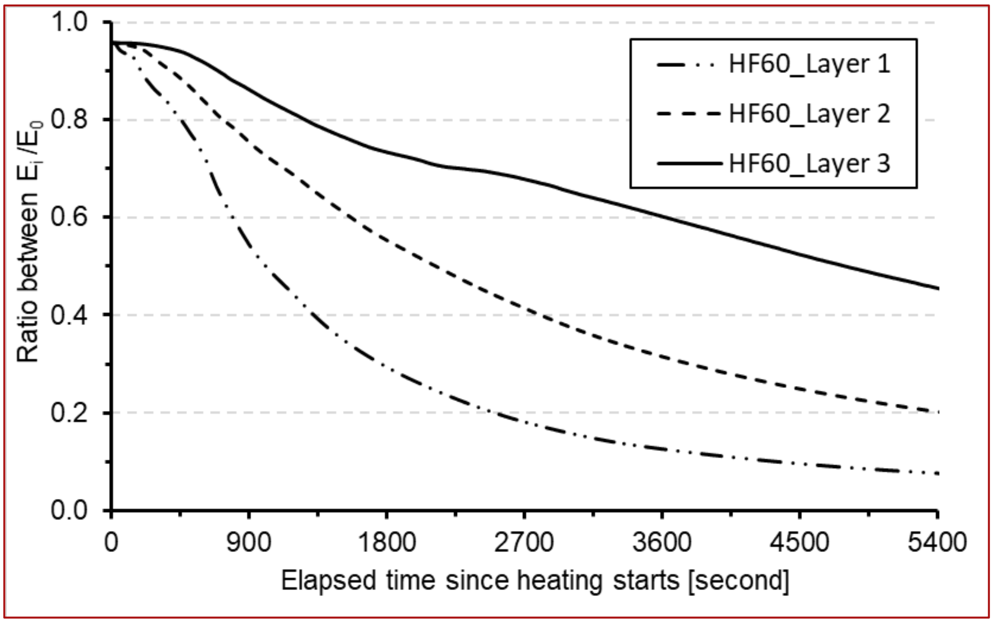

b) HF60

Figure 9. Ratio of average Young's modulus of each layer to E_0.

4. Results and discussions

In this section, the thermal reaction forces developed in the profiled composite walls are calculated for the case of a pinned-pinned restrained condition (Figure 5), which was the structural boundary condition for the test specimens reported in this study. The results of the thermal reaction force development calculated by the analytical model are directly compared with the test data collected from the experimental program.

At the early stages of heating, the temperature gradient was significantly higher in the outer layer, while most parts of the cross-section remained cold. Thus, the mechanical properties of concrete on the heated region (i.e., compressive strength and Young's modulus) were significantly smaller compared to the cold region due to the effect of temperature [6]. Meanwhile, the heated region is a relatively small proportion of the whole cross-section. In the structural behaviour, the increase in temperature and temperature gradient resulted in thermal expansion and thermal bowing and, consequently, thermal stresses within the cross-section. The thermal stress profile also depends on the structural boundary condition, as discussed in Section 2. The reaction forces at the supports and the deflection of the structural elements can be then directly calculated.

The deflection behaviour of the PCWs subjected to one-sided heating can be predicted using Equation 36:

Equation 36 $$\delta_x(z) = \frac{M_T}{2\overline{EI}}(z^2 - z.L)$$

where $\overline{EI}$ is the average stiffness of the cross-section. When subjected to one-sided heating under the pinned-pinned structural boundary condition, the PCW deflects toward the heating source with the highest deflection in the middle height of the PCW. The deflection of PCW depends on the combined effects of temperature gradient and temperature within sample's cross-section. As the temperature within PCWs' cross-section increases, the thermal moment M_T also increases while the average stiffness of PCW reduces. The deflection of PCW, thus, increases significantly at the early heating stage, then might remain stable when the temperature within the cross-section of PCW reaches the steady-state.

Figures 10 to 14 show the comparison between the calculated and measured thermal expansion forces of PCWs during the heating period of 90 min. Figures 10 and 11 show the results of the thermal expansion force developed in samples heated by HF42 and HF60 with no initial compressive loading in the case of pinned-pinned end conditions. While the calculated thermal expansion forces are much higher than those measured in samples heated by HF42, the calculated thermal expansion force is much smaller than those measured in samples heated by HF60. However, when the initial compressive load is applied on samples before heating ($0.2N_u^{amb}$ *and* $0.4N_u^{amb}$), the results calculated by the analytical model seem to agree well with the measured thermal expansion force developed in samples as shown from Figures 12 to 14.

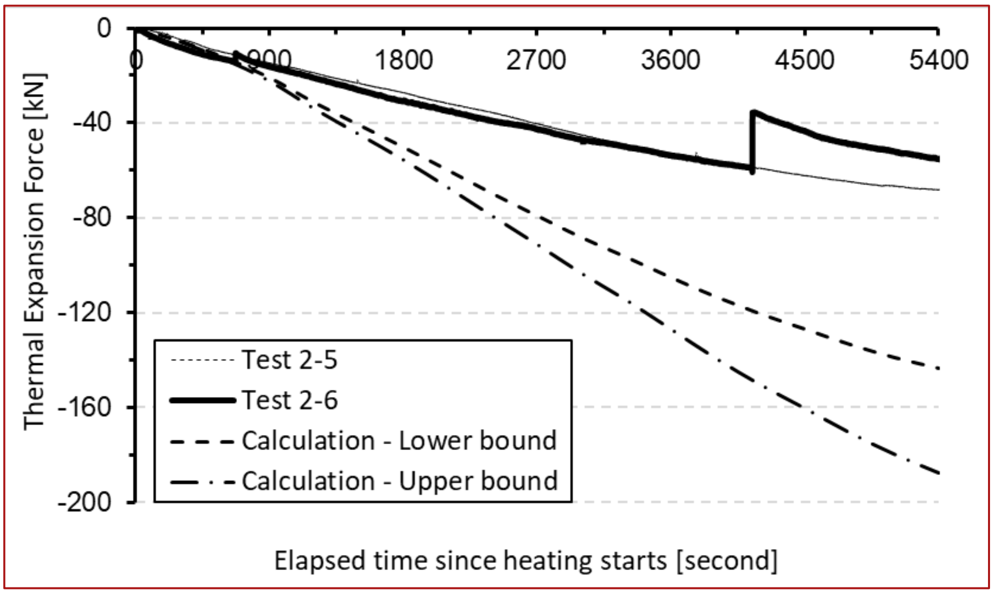

Figure 10. Comparison between predicted and recorded thermal expansion forces in Tests 2-5 and 2-6 collected from Le et al [26].

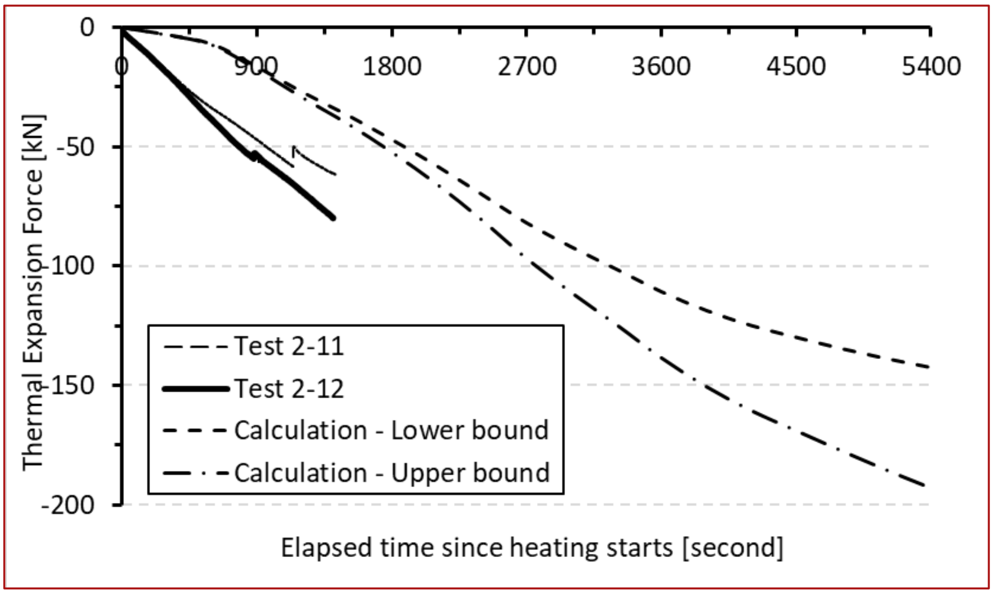

Figure 11. Comparison between predicted and recorded thermal expansion forces in Tests 2-11 and 2-12 (HF60 and P0) collected from Le et al [26].

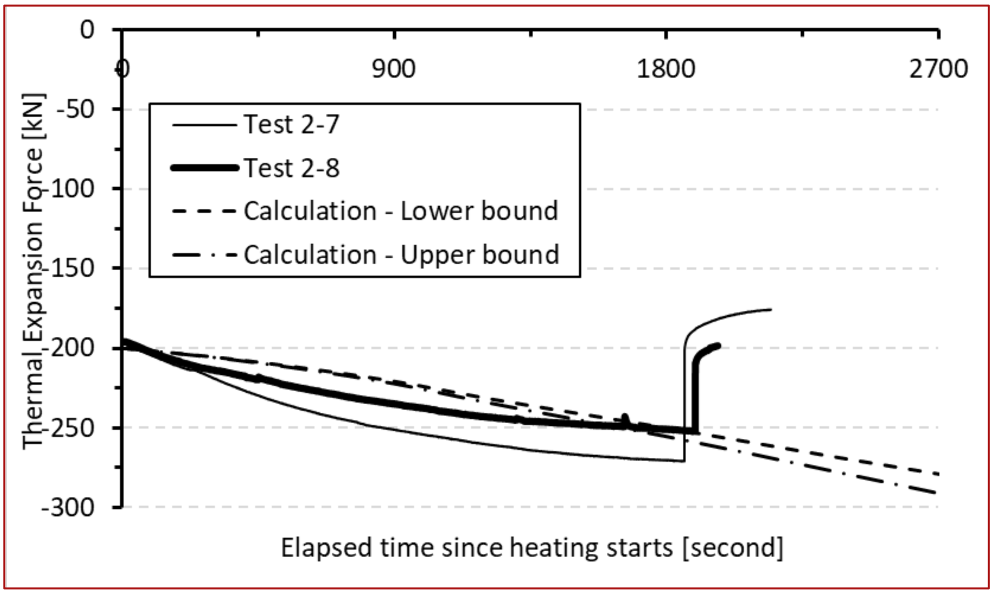

Figure 12. Comparison between predicted and recorded thermal expansion forces in Tests 2-7 and 2-8 (HF42 and P40) collected from Le et al [26].

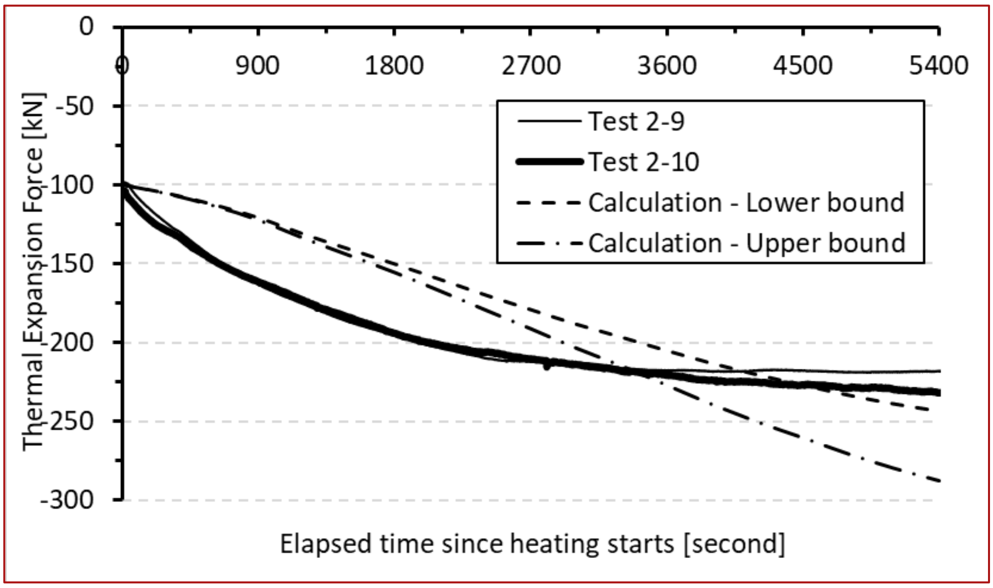

Figure 13. Comparison between predicted and recorded thermal expansion forces in Tests 2-9 and 2-10 (HF42, P20 and E10) collected from Le et al [26].

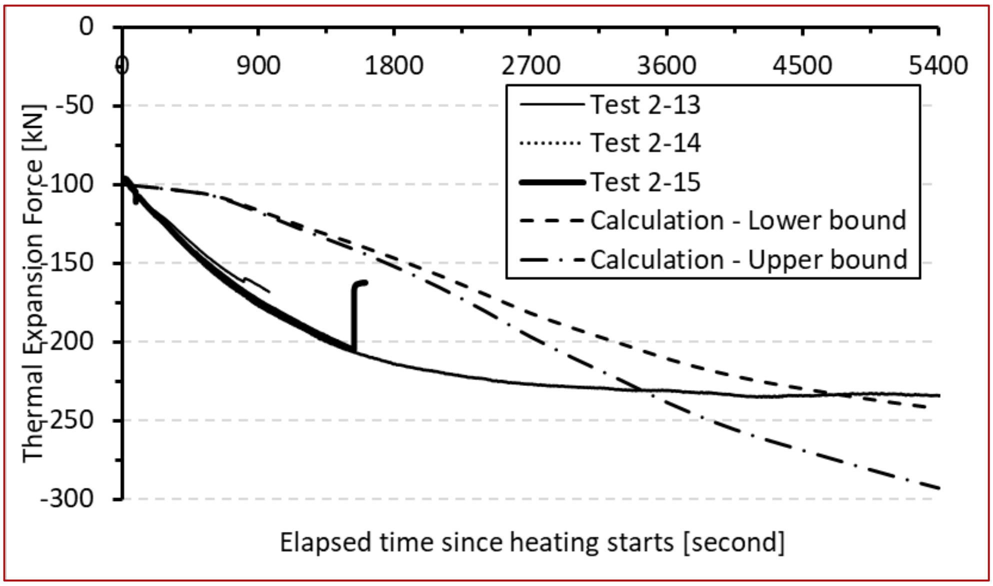

Figure 14. Comparison between predicted and recorded thermal expansion forces in Tests 2-13, 2-14 and 2-15 (HF60, P20 and E10) collected from Le et al [26].

It should be noted that the difference between the predicted and measured values in samples heated with no initial compressive loading (Figures 10 and 11) could be due to the poor contact conditions between the loading actuator and samples' surface during the experiment. Despite attempts to create samples with flat and parallel ends, the shrinkage of the concrete core during curing could have resulted in gaps between the samples' ends and actuator's surfaces. The effects of such gaps have been minimised in cases of initial compressive loading before heating (Figures 12 to 14). The remaining difference between the predicted and measured values in samples subjected to initial load before heating might be because the expansion force component contributed by the thin steel skin at the beginning of the heating procedure is neglected. Neglecting the expansion force simplifies the behaviour of the PCWs, especially when the profiled steel sheet is heated by a high incident heat flux of 60 kW/m^2.

Furthermore, the effect of spalling has not been explicitly captured in the model even though concrete spalling could affect the accuracy of the proposed model. The effects of spalling can be seen in some of the tests. For example, a significant loss of force can be seen at the heating time of 1800 s in Figure 12. This loss of thermal expansion force is due to of spalling which results in an effective loss of cross-section.

The agreement between the predicted and measured thermal expansion forces clearly indicates that key factors influencing the performance of PCWs at elevated temperatures have been adequately incorporated into the developed analytical model. By simultaneously taking into account the combined effects of thermal expansion, thermal bowing, coupled effects between stress and thermal expansion, and the shift of the effective centroid, the results suggest that the approach is capable of capturing the performance of structural elements subjected to temperature and temperature gradient during the heating stage.

It should be noted that the structural performance model in this paper is not developed by best fitting a mathematical function to the collected data. Prior to this work, these correlations were the norm. Although such correlations could be used to predict the performance of structural elements, their capacity and applicability range are limited to the collected data or characteristics of the experiments. These correlations are essentially mathematical fits that lack a rational basis. The difference between the present approach and the existing correlations is explained in detail in the following references [2, 11, 30].

These findings demonstrate that the thermal strain could be linearly combined using thermal expansion strain and thermal bowing strain over the whole cross-section while complying with the Bernoulli-Euler theory for strain compatibility. On the other hand, the strain of each fibre must be considered in the coupled effect between stress and thermal expansion through the load-induced thermal strain because of the presence of stress and temperature increase in each fibre [31]. The coupled effects could be considered by using a physically-based model developed for solid materials subjected to load and temperature change simultaneously [9, 11]. Also, the resulting stress profile must comply with the equilibrium of the applied load and resulting moment depending on the structural boundary conditions with respect to the change of effective centroid of the cross-section.

The shift of the effective centroid should be, therefore, carefully investigated when the Young's modulus is not uniformly distributed within the cross-section. The converted cross-section method seems to be an effective tool to evaluate the performance of structural elements subjected to elevated temperatures. Despite the success demonstrated through the thermal expansion force, this method has a limitation of dividing the cross-section into layers because concrete is a composite material where the size of aggregate could be a significant factor that affects the size of each layer. The in-depth temperature profiles at different heating times needs to be carefully analysed because there is no compatibility between a layer thickness defined by the maximum size of aggregate and layer thicknesses defined by the evolution of the temperature distribution in-depth of the sample. This inherent incompatibility will result in errors on the stress profile and subsequent shear stress value at the intersection zone between the layers.

Figure 15 shows the calculated stress profiles within cross-section of the PCWs at different heating times. The whole cross-section of PCWs subjected to compressive stress due to the restraint condition while temperature increases. By dividing the sample's cross-section into three composite layers joined by Bernoulli-Euler strain compatibility condition, the stress development within the cross-section depends on the temperature and Young's modulus of each concrete layer. Also, due to the difference of Young’s modulus among layers, there are steep changes of thermal stress at the interface between layers as shown in Figure 15. This steep change of thermal stress could be considered as thermal shear stress that might be the main factor governing the spalling behaviour of concrete.

It is clear that the model does not explicitly consider the complex impact of spalling on the stress profile across sample’s cross-section. Nevertheless, the model has correctly captured the trend and magnitude of the thermal expansion force when PCWs are subjected to thermal and mechanical loadings at the same time. By dividing the cross-section into layers, see Figure 15, the model provides a methodology to estimate the stress difference at the interface between layers. Such stress difference can then be used to compare with the tensile strength of concrete at elevated temperatures and qualitatively characterize the onset of spalling.

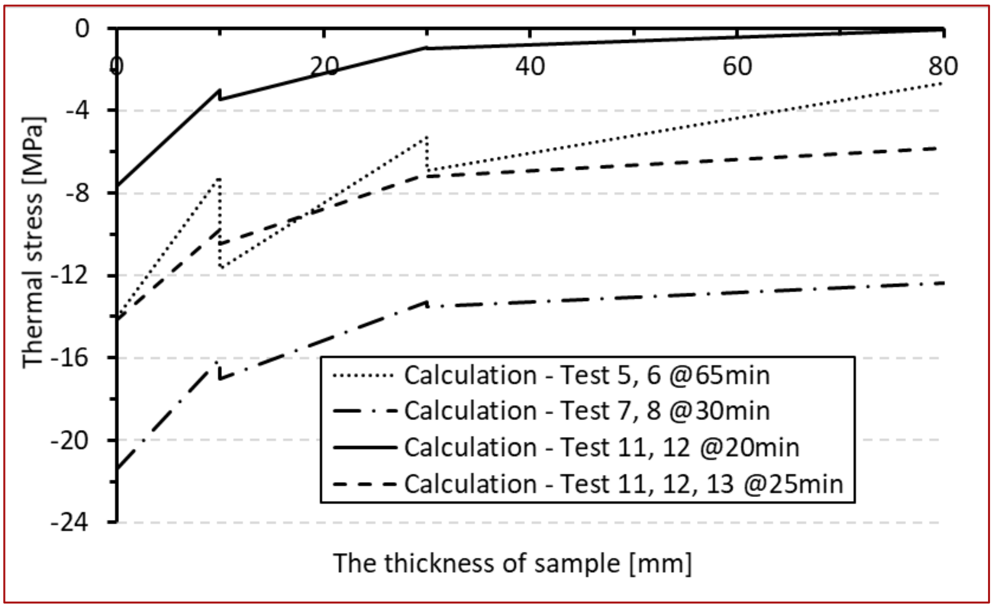

Figure 15. Predicted stress profiles in samples heated by different incident heat fluxes at different heating time.

This discussion relies on the assumption that the structural element complies with the Bernoulli-Euler theory, which creates a conservative calculation of thermal stresses developed in the cross-section. No experimental data exists showing the strain profile of the cross-sectional plane to determine whether it follows (i) Bernoulli-Euler theory, (ii) Timoshenko theory, or (iii) Higher-order strain profiles.

5. Summary and conclusions

In this paper, the developed analytical model has adequately considered the non-uniform evolution of temperature within the cross-section of structural elements subjected to one-sided heating and initial axial loading conditions. The load-induced thermal strain of concrete has been fully incorporated into the total strain model using a physically-based model. The combined effects of temperature and temperature gradient have been adequately considered while fulfilling the strain compatibility condition of Bernoulli-Euler theory between the different layers and for the whole cross-section. In addition, the effects of non-uniform Young's modulus distribution within the cross-section have been quantified by the shift of the effective centroid plane towards the colder region of the cross-section. Thus, the thermal expansion and bowing effects of the structural elements have been adequately addressed.

The analytical model requires the breakdown of the cross-section into layers that have different Young's modulus. It was shown that three layers were sufficient to capture all effects with adequate precision for the case of PCWs. The good agreement of thermal expansion forces between the analytical model and the collected experimental results highlights that the analytical model incorporates all the required phenomena. The model has correctly incorporated the key underlying physics and influencing factors to the performance of structural elements subjected to thermal-mechanical loading, including the combined effects of temperature and temperature gradient, the coupled effects between stress and thermal expansion, and the shift of effective centroid due to the non-uniform Young's modulus distribution within the cross-section.

It should be noted that the analytical model was developed invoking several assumptions. These assumptions include considering the effects of the heated steel sheet negligible. Therefore, the complexity of the performance of the PCWs was slightly reduced. While valid for the present systems, further studies should focus on understanding the limits of these assumptions when modelling the generalised performance PCWs at elevated temperatures.

This paper attempts to describe the complex physical behaviour of a structural element, thus the newly-developed model is a first attempt at incorporating significant features that have not been observed before. More work that needs to be conducted to develop a sufficiently precise model and the experiments that will serve to provide quantitative validation to the model.

Acknowledgements

The financial support of the Australian Research Council through LP140100504 and DP150102354 grants is gratefully acknowledged. This research is also funded by Funds for Science and Technology Development of the University of Danang under project number B2020-DN02-78.

Declaration of Competing Interest

The authors declare that they have no known competing financial interests or personal relationships that could have appeared to influence the work reported in this paper.

References

1. Torero, J., *Assessing the performance of concrete structures in fires.* Concrete in Australia - Special Issue on "Concrete Performance in Fire", 2014. **40**(3): p. 44-49.
2. Le, Q.X., et al., *Effects of temperature and temperature gradient on concrete performance at elevated temperatures.* Advances in Structural Engineering, 2018. **21**(8): p. 1223-1233.
3. Fletcher, I.A., et al., *Behaviour of concrete structures in fire.* Thermal science, 2007. **11**(2): p. 37-52.
4. Kodur, V.K.R. and M.A. Sultan, *Effect of temperature on thermal properties of high-strength concrete.* Journal Of Materials In Civil Engineering, 2003. **15**(2): p. 101-107.
5. Phan, L.T., *Fire performance of high-strength concrete: A report of the state-of-the-art.* The National Institute of Standards and Technology (NIST), 1996: p. 118.
6. European Standard, *Eurocode 2: Design of concrete structures. ENV 1992: Part 1-2: General rules - Structure fire design*, in *EN 1992-1-2 (2004): Eurocode 2: Design of concrete structures - Part 1-2: General rules - Structural fire design*. 2004, European committee for Standardization: Brussiles, Belgium.
7. Usmani, A.S., et al., *Fundamental principles of structural behaviour under thermal effects.* Fire Safety Journal, 2001. **36**(8): p. 721-744.
8. Garlock, M. and S. Quiel, *Mechanics of wide-flanged steel sections that develop thermal gradients due to fire exposure.* International Journal of Steel Structures, 2007. **7**: p. 153-162.
9. Pham, D.T., et al., *Yield design-based analysis of high rise concrete walls subjected to fire loading conditions.* Engineering Structures, 2015. **87**: p. 153-161.
10. Gernay, T., *Effect of transient creep strain model on the behavior of concrete columns subjected to heating and cooling.* Fire Technology, 2012. **48**: p. 313-329.
11. Le, Q.X., J.L. Torero, and V.T.N. Dao, *Understanding the effects of stress on the coefficient of thermal expansion.* International Journal of Engineering Science, 2019. **141**: p. 83-94.
12. Gernay T and Franssen JM, *Consideration of transient creep in the Eurocode constitutive model for concrete in the fire situation.* Proceedings of The Sixth International Conference Structures in Fire, 2010: p. 784-791.

13. Anderberg, Y. and S. Thelandersson, *Stress and deformation characteristics of concrete at high temperatures. 2. Experimental investigation and material behaviour model*. Vol. Bulletin 54. 1976: Lund Institute of Technology. 86.
14. Khoury, G.A., B.N. Grainger, and P.J.E. Sullivan, *Transient thermal strain of concrete: literature review, conditions within specimen and behaviour of individual constituents.* Magazine of Concrete Research, 1985. **37**(132): p. 131-144.
15. Khoury, G.A., B.N. Grainger, and P.J.E. Sullivan, *Strain of concrete during first heating to 600°C under load.* Magazine of Concrete Research, 1985. **37**(133): p. 195-215.
16. Khoury, G.A., W.P. Dias, and P.J.E. Sullivan, *Deformation of concrete and cement paste loaded at constant temperatures from 140 to 724°C.* Materials and Structures, 1986. **19**(2): p. 97-104.
17. Hossain, K.M.A., L.K. Mol, and M.S. Anwar, *Axial load behaviour of pierced profiled composite walls with strength enhancement devices.* Journal of Constructional Steel Research, 2015. **110**: p. 48-64.
18. Rafiei, S., et al., *Profiled sandwich composite wall with high performance concrete subjected to monotonic shear.* Journal of Constructional Steel Research, 2015. **107**: p. 124-136.
19. Rafiei, S., et al., *Finite element modeling of double skin profiled composite shear wall system under in-plane loadings.* Engineering Structures, 2013. **56**: p. 46-57.
20. Taormina, A. and K.M.A. Hossain, *Behaviour of profiled composite walling system under elevated temperatures*, in *Annual Conference of The Canadian Society for Civil Engineering 2012 : Leadership In Sustainable Infrastructure*, CSCE, Editor. 2012, Canadian Society for Civil Engineering Montreal: Edmonton, Alberta, Canada.
21. Torero, J.L., A. Law, and C. Maluk, *Defining the thermal boundary condition for protective structures in fire.* Engineering Structures, 2017. **149**: p. 104-112.
22. Hetnarski, R.B., *Encyclopedia of Thermal Stresses*, ed. R.B. Hetnarski. 2014, Dordrecht: Springer.
23. Hetnarski, R.B., M.R. Eslami, and G.M.L. Gladwell, *Thermal stresses: Advanced theory and applications*. 2009: Dordrecht: Springer Netherlands.
24. Obata, Y., *Beams, Thermal stresses*, in *Encyclopedia of Thermal Stresses*, R.B. Hetnarski, Editor. 2014, Springer: Dordrecht. p. 365-372.
25. Malzbender, J., *Mechanical and thermal stresses in multilayered materials.* Journal of Applied Physics, 2004. **95**(4): p. 1780-1782.
26. Le, Q.X., et al., *Experimental study into the behaviour of profiled composite walls under combined axial and thermal loadings.* Engineering Structures, 2020. **210**: p. 110354.
27. Welch, S., et al., *BRE large compartment fire tests—Characterising post-flashover fires for model validation.* Fire safety Journal, 2007. **42**: p. 548-567.
28. Aslani, F. and M. Bastami, *Constitutive relationships for normal-and high-strength concrete at elevated temperatures.* ACI Materials Journal 2011. **108**(4): p. 355-364.
29. Diederichs, U., U.M. Jumppanen, and V. Penttala, *Material properties of high strength concrete at elevated temperatures*, in *IABSE 13 Congress*. 1988: Helsinki.
30. Le, Q.X., J.L. Torero, and V.T.N. Dao, *Stress–strain–temperature relationship for concrete.* Fire Safety Journal, 2020: p. 103126.
31. Rosenfield, A.R. and B.L. Averbach, *Effect of stress on the thermal expansion coefficient.* Journal of Applied Physics, 1956. **27**(2): p. 154-156.